

Boundary-fitted numerical model for computing linear and nonlinear wave forces on bottom-mounted piles

B. Barlas*, S. Beji

Faculty of Naval Architecture and Ocean Engineering, Istanbul Technical University, Maslak 34469, Istanbul, Turkey

Received 31 May 2006; received in revised form 21 November 2006; accepted 8 January 2007

Available online 20 February 2007

Abstract

A vertically-integrated nonlinear dispersive wave model in nonorthogonal curvilinear coordinate system is used for simulating linear and nonlinear wave forces on bottom mounted circular and elliptical piles. The wave model is in terms of the contravariant velocities hence the wall condition for arbitrarily shaped objects is satisfied accurately and easily. As basic test cases, computations of linear wave forces on vertical cylinders of circular and elliptical cross sections are compared with the available analytical results. Cnoidal waves incident on circular and elliptical cylinders are also simulated for different wave steepness ratios and wave shape parameter values to observe the effect of nonlinearity and wave form. Comparisons of linear and nonlinear force coefficients and relevant discussion are presented in closing.

© 2007 Elsevier Ltd. All rights reserved.

Keywords: Boundary-fitted coordinates; Vertically integrated equations; Linear and nonlinear wave forces

1. Introduction

Reliable estimation of wave and current induced forces on a sea structure constitutes probably the most important part of a design project. Almost exclusive use of circular cylinders as principal structural components necessarily places circular piles in the center of most research work. Havelock [1] was the first to formulate the linear diffraction theory for a vertical circular cylinder in deep water conditions. Omer and Hall's work [2] may be viewed as the shallow water version of Havelock's work. Finally MacCamy and Fuchs [3] generalized the theory for finite depth conditions. Due to obvious theoretical difficulties, analytical treatments of different cross-sectional shapes are rare. Goda and Yoshimura's [4] formulation of wave forces on a vertical pile of elliptic cross-section may be addressed as a notable exception.

With the advent of computational facilities and numerical techniques the problems beyond the power of analytical methods have begun receiving attention. Houston [5] employed the finite-element technique for the combined refraction–diffraction problem, Chau and Eatock Taylor [7] and

Isaacson and Cheung [6] studied the nonlinear wave diffraction for a Stokes second-order wave field while Jiang and Wang [8] used a generalized Boussinesq model for modelling the interactions of cnoidal waves with a vertical cylinder. Later, Wang and Ren [9] extended the work of Jiang and Wang [8] to an array of cylinders. An accurate boundary element model for the calculation of wave loads on multiple circular cylinders was given by Zhu and Moule [10]. Stojek et al. [11] used Trefftz-type finite elements for the computation of wave loads on a group of vertical cylinders with rectangular cross-section. On the experimental side, works of Kyte and Tørum [12] on vertical cylinders placed on shoals, Huseby and Grue [13] on higher-harmonic wave forces, and Morris-Thomas and Thiagarajan [14] on the harmonic components of the run-up may be mentioned as recent contributions to the subject.

The present work uses a vertically integrated nonlinear-dispersive wave model expressed in curvilinear coordinates in terms of the contravariant velocities. The wave equations in generalized coordinates are numerically solved using finite-difference approximations with staggered grids. Only half of the circular or elliptical cylinder about the symmetry axis is placed inside the physical domain so that the computational domain becomes a perfect rectangle without any effort. Multiple cylinders may also be considered if a dual-grid

* Corresponding author.

E-mail addresses: barlas@itu.edu.tr (B. Barlas), sbeji@itu.edu.tr (S. Beji).

technique is adopted as in Wang and Ren [9]. Due to the hyperbolic form of the velocity profile the evanescent modes are not fully accounted for, but the Galerkin type formulation of the original wave model indicates that these effects may be compensated to some degree as vertical velocity profiles of differing wave numbers are approximated quite satisfactorily (see Nadaoka et al. [15] for details).

The outline of the paper is as follows. The next section gives a brief description of the problem considered. Section 3 introduces the wave model and describes the numerical solution technique for the problem in hand. In Section 4 linear wave force computations for circular cylinders are performed first and repeated for elliptical cylinders as benchmark tests to check the accuracy of the model equations and the numerical scheme. The computed dimensionless force maxima are plotted against the theoretical values given by the linear theory of MacCamy and Fuchs [3] for circular cylinders and by the analytical results of Goda and Yoshimura [4] for elliptic cylinders. In Section 5 the effects of nonlinearity are investigated using cnoidal waves of two different steepness ratios and two different elliptic modulus values. Again the computed dimensionless nonlinear force maxima are compared with each other and with the corresponding linear analytical values. The most remarkable outcome of the nonlinear computations for both circular and elliptical cross sections is that the effect of nonlinearity is quite pronounced in the weak diffraction regime whereas the opposite is the case in the strong diffraction regime. Such a general trend appears to be supported by experimental findings as well [16,17]. Furthermore, the wave shape quantified by the elliptic modulus m for cnoidal waves is observed to play an appreciable role too. Higher elliptic modulus values which indicate narrower cnoidal wave profiles produce higher dimensionless forces thus revealing that nonlinear force magnitudes depend not only on the wave steepness but also on the wave form.

2. Problem description

The present work considers the numerical computation of horizontal wave forces acting on bottom-mounted piles of circular and elliptical cross sections with diffraction effects. Fig. 1 depicts the side view and plan view of the problem with coordinate system used. The incident waves are introduced from the left at $x = 0$ along the y -axis. The cylinder is placed at $0.6L$, to the right of the mid-domain, to delay the contaminating effects of the reflected waves traveling back to the incoming boundary. The end of the domain $x = L$ is designated as an open boundary by implementing an appropriate radiation condition.

The numerical solution is carried out using a boundary-fitted model hence the corresponding computational domain is perfectly rectangular. Fig. 2 shows a typical grid arrangement for the physical domain in the (x, y) coordinates and its counterpart in the computational domain in the (ξ, η) coordinates. The boundary-fitted model is formulated for nonorthogonal grids, hence no special care is needed for generating orthogonal grids. While the grid sizes in the physical

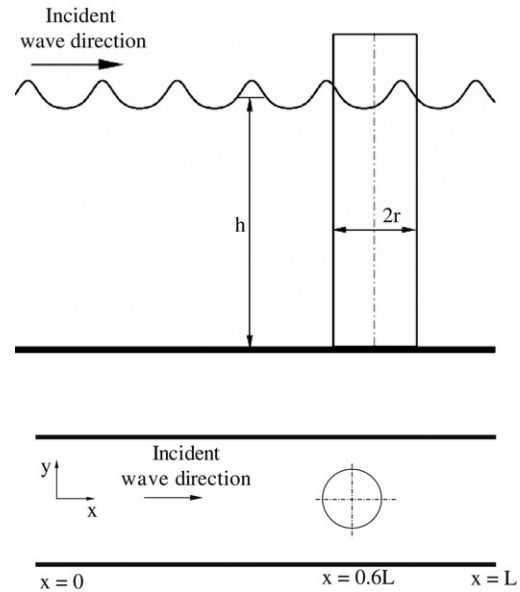


Fig. 1. Side view and plan view of the problem for a circular cylinder.

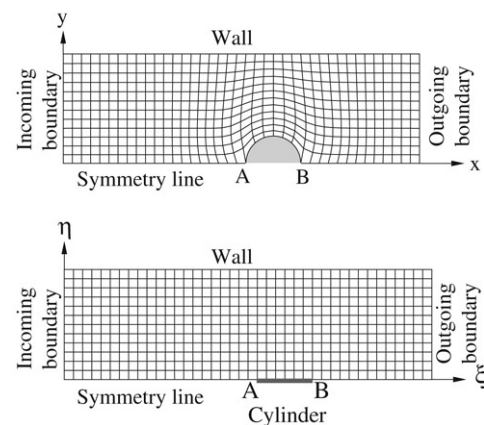


Fig. 2. A typical grid arrangement in the physical domain (x, y) and its counterpart in the computational domain (ξ, η) for a circular cylinder.

domain vary depending on the location, the grid sizes in the computational domain are taken as unity in both ξ - and η -directions for numerical efficiency. Due to the symmetry of the problem only half of the domain is discretized.

3. Wave model, boundary conditions and numerical approach

3.1. Boundary-fitted wave model

The wave model used in this work is the one-component form of the fully-dispersive nonlinear model of Nadaoka et al. [15] as expressed in boundary-fitted coordinates by Beji and Barlas [18]. The model is operational for both shallow and deep water waves hence it can reproduce the cnoidal and the second-order Stokes waves equally well, besides simulating narrow banded nonlinear random waves over arbitrary depths. In the curvilinear coordinate system (ξ, η) the continuity equation and ξ - and η -components of the momentum equation

are given as [18]

$$\zeta_\tau + J \left[\left(C_p^2/g + \zeta \right) U^* \right]_\xi + J \left[\left(C_p^2/g + \zeta \right) V^* \right]_\eta = 0, \quad (1)$$

$$nJU_\tau^* + \xi_*^2 Q_\xi + \xi_* \eta_* Q_\eta = \frac{\xi_*^2}{\omega^2 C_p^2} \left[C_* \left(U_\xi^* + V_\eta^* \right) \right]_{\xi\tau} + \frac{\xi_* \eta_*}{\omega^2 C_p^2} \left[C_* \left(U_\xi^* + V_\eta^* \right) \right]_{\eta\tau}, \quad (2)$$

$$nJV_\tau^* + \xi_* \eta_* Q_\xi + \eta_*^2 Q_\eta = \frac{\xi_* \eta_*}{\omega^2 C_p^2} \left[C_* \left(U_\xi^* + V_\eta^* \right) \right]_{\xi\tau} + \frac{\eta_*^2}{\omega^2 C_p^2} \left[C_* \left(U_\xi^* + V_\eta^* \right) \right]_{\eta\tau}, \quad (3)$$

with

$$Q = g\zeta + \frac{1}{2} \left(1 - 3\omega^2 C_p^2/g^2 \right) \times \left[\eta_*^2 U^{*2} + \xi_*^2 V^{*2} - 2\xi_* \eta_* U^* V^* \right]$$

$$\xi_*^2 = \xi_x^2 + \xi_y^2, \quad \eta_*^2 = \eta_x^2 + \eta_y^2,$$

$$\xi_* \eta_* = \xi_x \eta_x + \xi_y \eta_y, \quad C_* = C_p^4 (1 - n) J$$

where g is the gravitational acceleration, ζ is free surface elevation, U and V are the contravariant components of the horizontal velocity vector at $z = 0$ with $U^* = U/J$ and $V^* = V/J$. J is the Jacobian and $\xi_x, \xi_y, \eta_x, \eta_y$ are the metrics of the transformation. $n = C_g/C_p$ with C_p and C_g denoting respectively the phase and group velocities computed according to linear theory for a specified wave frequency ω and a given local depth h . Subscripts indicate partial differentiation with respect to the indicated variable with subscript τ denoting time in the curvilinear coordinates.

3.2. Boundary conditions

At any given point the contravariant velocities (U, V) are in the (ξ, η) directions; therefore, even for irregular geometries, the wall condition may be specified quite simply by requiring the contravariant velocity component normal to the wall boundary vanish.

At the incoming boundary the form of the incident waves are specified as either sinusoidal or cnoidal, the sinusoidal form being used for linear simulations. For sinusoidal waves the corresponding linear velocity U is obtained from the linearized continuity equation as $U = \zeta C/(C_p^2/g)$ with C being the phase velocity of the incident wave. The phase velocity C_p used in the model is always taken equal to C for accurate simulations. The cnoidal wave form is taken from the classical theory of Korteweg and de Vries [19] as described in [20]. The nonlinear horizontal velocity in the ξ -direction is obtained from the full form of the continuity equation as $U = \zeta C/(C_p^2/g + \zeta)$ with C denoting the cnoidal wave celerity.

In principle the wave equations may be used on the open boundaries too. However, the discretization must be one-sided to prevent overlapping outside the intended computational region. Also, typically tri-diagonal form of the unknown velocity matrix becomes modified. Despite these disadvantages

use of wave equations on the open boundaries improves the radiation of the nonlinear waves significantly as demonstrated in [21]. In curvilinear coordinates the momentum equations necessarily contain more terms than their cartesian forms do, therefore use of the boundary-fitted equations on the open boundaries becomes quite a complicated application. For this reason, the usual approach is adopted here and Sommerfeld's classical radiation condition is employed. For directional waves higher-order boundary conditions, such as suggested by Engquist and Majda [22] may be used for better absorption of complicated wave patterns. However, even for directional waves, Sommerfeld's condition in boundary-fitted coordinates is found to give quite acceptable results. For waves moving in the positive ξ -direction Sommerfeld's equation in curvilinear coordinates is given by [18]

$$\begin{aligned} & (\xi_x \eta_y - \xi_y \eta_x) U_\tau^* \\ & + C \left[\left(\xi_x^2 \eta_y - \xi_y^2 \eta_x \right) U_\xi^* + \eta_x \eta_y (\xi_x - \xi_y) U_\eta^* \right] \\ & + C \xi_x \xi_y \left[(\xi_y - \xi_x) V_\xi^* + (\eta_y - \eta_x) V_\eta^* \right] = 0. \end{aligned} \quad (4)$$

If the physical domain is rectangular, $\xi_x = 1, \xi_y = 0, \eta_x = 0$, and $\eta_y = 1$, the above equation reduces to $u_t + Cu_x = 0$, which is the usual form.

3.3. Numerical approach

Since the computational domain is always rectangular, the numerical solution of the transformed wave equations may be carried out conveniently using finite-difference approximations. Discretization of the computational domain follows the Arakawa C-grid scheme [23]. The choice of the Arakawa C-grid is not arbitrary, the final selection has been made from among three different grid schemes which were tested previously in [18].

The time derivatives are centred at the mid-time level $t + \Delta t/2$, t being the current time and Δt the time step. The wave propagation direction is taken along the positive ξ -axis; therefore, ξ -momentum equation is solved first to obtain U^* for the new time level $t + \Delta t$, assuming the new time level values of ζ and V^* known. Then, η -momentum equation is solved for V^* using U^* as computed from the previous step. Finally, the surface displacement is obtained from a semi-explicit discretization of the continuity equation. Since all these computations involve certain approximations, an iterative procedure is necessary. Through numerical experiments it has been ascertained that five iterations are sufficient to obtain reliable results. This number was determined by checking the values of the variables at selected locations between successive iterations until the difference between two consecutive iterations became less than a specified small value 10^{-5} . Complete details of the numerical approach can be found in Beji and Barlas [18].

4. Linear wave forces

Simulations of linear wave forces for both circular and elliptical cylinders provide quantitative estimates for the

accuracy of the model predictions through comparisons with the analytical solutions which are available for these particular cross-sectional forms.

4.1. Circular cross-section

The analytical solution of the linearized diffraction problem for a circular cylinder at arbitrary water depths was given by MacCamy and Fuchs [3]. Accordingly, the nondimensional maximum horizontal force \bar{F}_{\max} is

$$\bar{F}_{\max} = \frac{F_{\max}}{\rho g h H r (\tanh kh / kh)} = 2 \frac{[J_1'^2(kr) + Y_1'^2(kr)]^{-1/2}}{kr}, \quad (5)$$

where ρ is the water density, h the water depth, k the wave number, H the incident wave height, r the cylinder radius, and $J_1'(kr)$ and $Y_1'(kr)$ are derivatives of the Bessel's functions of the first and second kind of the order one.

As schematized in Fig. 2 numerical computations are performed for half of the physical domain cut through the symmetry line. The incident boundary condition is specified as a simple sinusoidal wave while the outgoing boundary is specified according to Eq. (4) as a nonreflecting boundary. The wall condition is imposed along the upper wall and the symmetry line.

For wave simulation problems it is customary to use a fixed resolution in the wave propagation direction as a fraction of the incident wavelength. However, the present problem has two independent length scales: the incident wavelength and the cylinder radius. By changing the magnitude of the one relative to the other, different kr values are simulated; therefore, it is not possible to fix the resolution in the x -direction as a definite fraction of the incident wavelength. If kr is small, the resolution, which is sufficient for the incident wave, is usually insufficient for resolving the cylinder. Likewise, if kr is large, the resolution which is satisfactory for the cylinder is unsatisfactory for the wavelength. Only for the specific value of $kr = \pi$ for which both length scales become identical $2r = \lambda$, the resolution of the two scales becomes identical (a definite resolution results in identical resolutions for both the wave and the cylinder).

Due to the conflicting aspects of the problem, especially for small and large kr values, it is necessary to adopt a compromising approach to reconcile the different resolutions. First, for simplicity, the water depth is taken to be $h = 1$ m and the wavelength $\lambda = 2\pi$ m for all simulations. The corresponding incident wave period is thus fixed just like the incident wavelength and water depth and obtained from the dispersion relation as $T = 2\pi / \sqrt{g \tanh(1)} \simeq 2.3$ s. Since kr is the principal non-dimensional parameter indicating the extent of diffraction, a range of $kr = 0.4$ – 2.4 values with increments of 0.2 is used to determine the cylinder radius which is varied again between $r = 0.4$ and 2.4 since $k = 1$ for $\lambda = 2\pi$. Then, a typical physical domain length $L = 10\lambda = 20\pi$ and width $W = 10r$ are defined. The width of the domain is especially kept wide enough to avoid the interference of the possible reflections from the wall. The resolution in the x -direction is

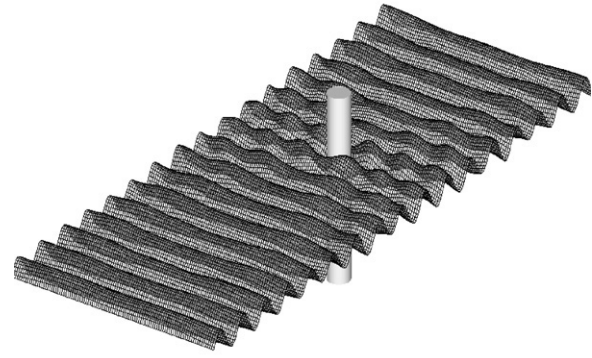


Fig. 3. Perspective view of a fully developed wave field at $t = 35T$ in presence of circular cylinder for $kr = 2.0$.

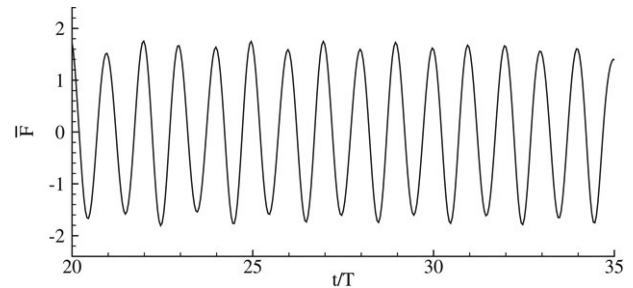


Fig. 4. Computed nondimensional linear wave force on circular cylinder for a duration of 15 periods between $t = 20T$ and $t = 35T$ for $kr = 2.0$.

defined as a fraction of the incident wavelength but it is not fixed and varied between $\Delta x = \lambda/25$ – $\lambda/80$ depending on the case, the resolution being lower for large kr and higher for small kr . The resolution in the y -direction is taken depend on Δx as $\Delta y = 1.5\Delta x$. Finally, the time step Δt is determined from the condition that the wave Courant number in the x -direction $C\Delta t/\Delta x$ be unity. Such a condition is not necessary but presumably gives more accurate results.

Sensitivity to the grid size is investigated systematically by performing three different computations for each case. After performing the computation for the typical domain length and grid size given above, the grid size is first increased and then decreased by 25% and the computations are repeated. Finally, all three results are averaged to get the final force magnitude for each kr . The minimum and maximum of the deviations from the mean are found to be respectively 6.0% for $kr = 0.4$ and 7.4% for $kr = 2.4$.

Fig. 3 shows a perspective view of a fully developed wave field in presence of the cylinder for $kr = 2.0$ after 35 wave periods elapsed from the start. Fig. 4 depicts a sample of the computed nondimensional force for a duration of 15 periods again for $kr = 2.0$. The wave force on the pile is computed from the numerical integration of the first integral (linear part) given by Eq. (A.8) in the Appendix.

In Fig. 5 numerically computed nondimensional force maxima are compared with the analytical solution given by Eq. (5) for 11 different values of $kr = 0.4$ – 2.4 . Overall the

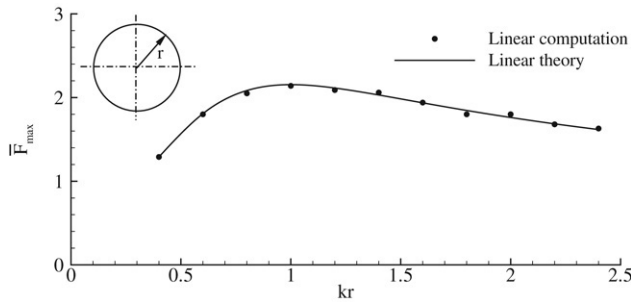


Fig. 5. Nondimensional force maxima on circular cylinder as predicted by linear theory (solid line) and computed using the wave model (full circles) for a range of kr values.

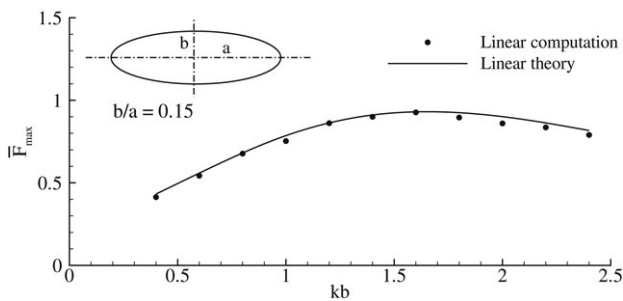


Fig. 6. Nondimensional force maxima on elliptical cylinder as predicted by the linear theoretical solution of Goda and Yoshimura (solid line) and computed using the wave model (full circles) for an elliptical cylinder with $b/a = 0.15$.

agreement is quite satisfactory with a maximum difference of 2.7% for $kr = 1.8$.

4.2. Elliptic cross-section

Goda and Yoshimura [4] analytically solved the problem of linear wave scattering by a vertical elliptical cylinder and calculated the wave forces acting on the cylinder. Their solution, which is expressed in terms of Mathieu functions and their derivatives, is valid for arbitrary short to long axis ratios and arbitrary wave directions. Reproduction of the complete solution is quite complicated therefore a sample case presented in their work is selected for comparisons. The simulated case is for $b/a = 0.15$ where a is the long and b is the short axis of the elliptical cross-section. The ellipse is aligned such that the long axis lies in the direction of wave propagation.

Numerical computations quite similar to those for the circular cylinder are performed again for 11 different values of $kb = 0.4$ – 2.4 . Naturally, b is now used as the length scale of diffraction effect in accord with Goda and Yoshimura [4]. The grid resolutions are arranged likewise; however, instead of the radius r , the long axis a is used for the x -direction quantities and the short axis b is used for the y -direction quantities. The wave force is nondimensionalized by using b in place of r . The resolution in the y -direction is $\Delta y = 1.5\Delta x$ as used for the circular cylinder. Fig. 6 shows the analytical solution given in [4] against the numerical results which are the mean values calculated from computations for three different resolutions as detailed in Section 4.1 for each kb . The numerically computed results are in good agreement with the analytical solution for

the entire range; the maximum difference is 4.9% for $kb = 2.0$. Thus, it may be safe to conclude that at least for linear simulations the present model gives quite reliable estimates of the wave forces.

5. Cnoidal wave forces

Korteweg and de Vries [19] used the word cnoidal for nonlinear periodic waves of permanent shape in shallow water. In order to investigate the effects of nonlinearity on the form and magnitude of the wave forces acting on vertical cylinders the cnoidal waves are now used as incident waves.

According to the cnoidal theory only two parameters may be selected freely; the rest of the physical wave quantities are determined in terms of these two parameters and the complete elliptic integrals of the first kind $K(m)$ and the second kind $E(m)$, which depend on the elliptic modulus m (see for instance Abramowitz and Stegun [24], p.590).

The presentation plan requires the selection of a definite wave steepness $\epsilon = H/h$ to measure the nonlinearity and an elliptic modulus m to quantify the wave form. In order to carry out this plan, two wave steepness values $\epsilon = 0.1, 0.3$ and two different elliptical modulus values $m = 0.90, 0.95$ are selected first. To avoid extremely high wave heights due to reflection in front of the pile the wave steepness values are kept within moderate limits. The water depth is fixed at $h = 0.25$ m, which allows the long wave condition to be satisfied for the wavelengths computed according to the formula $\lambda = 4hK(m)\sqrt{m/3\epsilon}$ as dictated by the classical cnoidal theory. The principal nondimensional parameter kr is varied between 0.4 and 2.4 as in the linear computations. For each case the cylinder radius is computed from $r = kr(\lambda/2\pi)$.

5.1. Circular cross-section

Cnoidal wave forces on circular piles are simulated first. The spatial and time resolutions used in the simulations basically follow their linear counterparts expect for the isolated cases with numerical instabilities due to nonlinearities. In such cases the resolutions are altered to avoid the numerical instabilities.

Fig. 7 shows a perspective view of a fully developed cnoidal wave field with $\epsilon = 0.3$ and $m = 0.90$ in presence of the circular cylinder for $kr = 1.0$. It may be compared with the linear case shown previously in Fig. 3. Likewise, the cnoidal counterpart of Fig. 4 is given in Fig. 8 again for $\epsilon = 0.3$, $m = 0.90$, and $kr = 1.0$. When compared with Fig. 4 the functional change of the force due to the presence of the bound harmonic components, which create an asymmetrical and skewed appearance, is quite pronounced. The cnoidal wave force on the pile is computed from the numerical integrations of the integrals given in (A.8).

In Fig. 9 numerically obtained nondimensional force maxima for $\epsilon = 0.1$ and for two different elliptical modulus values $m = 0.90$ and $m = 0.95$ are plotted. The linear solution is also included for reference. The results of a corresponding simulation for $\epsilon = 0.3$ are presented in Fig. 10. Both figures obviously indicate that the effect of nonlinearity increases with

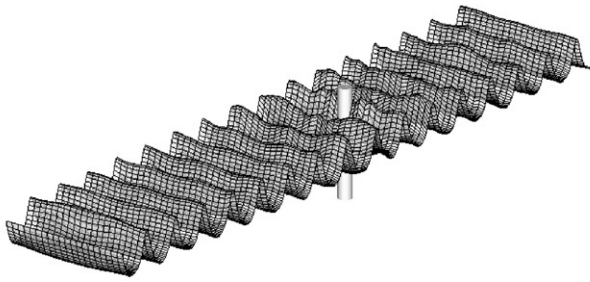


Fig. 7. Perspective view of a fully developed cnoidal wave field with $\epsilon = 0.3$, $m = 0.90$ at $t = 35T$ in presence of circular cylinder for $kr = 1.0$.

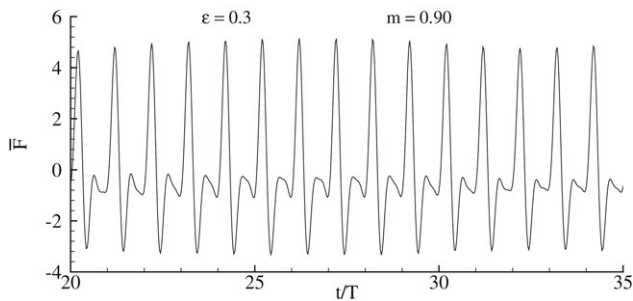


Fig. 8. Computed nondimensional cnoidal wave force on circular cylinder for a duration of 15 periods between $t = 20T$ and $t = 35T$ for $\epsilon = 0.3$, $m = 0.90$, and $kr = 1.0$.

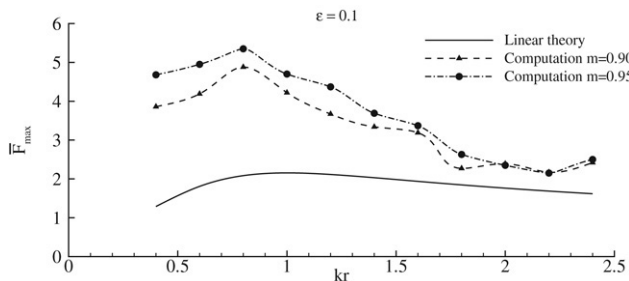


Fig. 9. Nondimensional cnoidal force maxima on circular cylinder for $m = 0.90$ (full triangles) and $m = 0.95$ (full circles) both for $\epsilon = 0.1$. Linear theory (solid line) is also plotted for reference.

decreasing diffraction effect. Such a trend is also supported by the computational results of Jiang and Wang [8] who simulated cnoidal wave forces using a Boussinesq model. It is to be noted that their nondimensionalization differs from the present work and therefore direct comparisons are not possible. Measurements reported in Kriebel [16], and in a different context the Stokes wave force simulations of Isaacson and Cheung [6] reveal parallel trends.

Besides the obvious dependency of nonlinear effect on kr , the shape of the cnoidal wave form, as quantified by the elliptic modulus m , appears to affect the force magnitude. Larger m values, which cause the wave form to become narrower, result in larger nondimensional force values. The reason may be related to the greater spatial gradients of orbital velocities, which in turn dictate the dynamic pressure. Being one of the nondimensional parameters defining cnoidal wave form, the elliptic modulus would naturally be expected to play a role in computations, though its significance may be argued. The

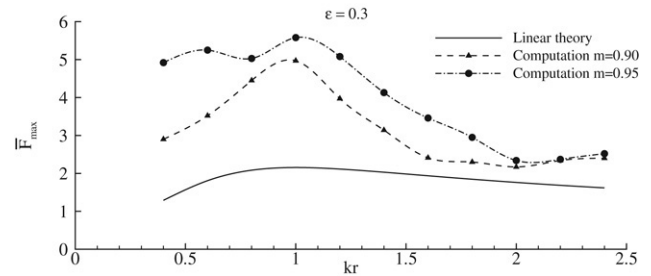


Fig. 10. Nondimensional cnoidal force maxima on circular cylinder for $m = 0.90$ (full triangles) and $m = 0.95$ (full circles) both for $\epsilon = 0.3$. Linear theory (solid line) is also plotted for reference.

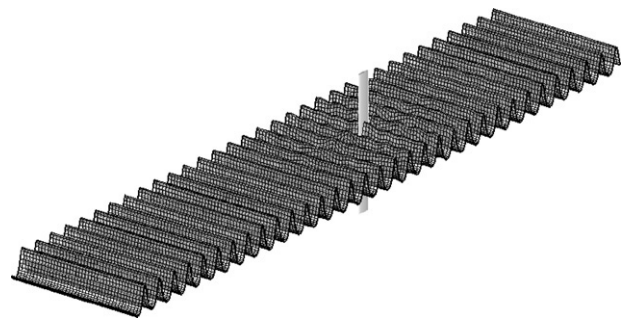


Fig. 11. Perspective view of a fully developed cnoidal wave field at $t = 44T$ in presence of elliptical cylinder ($b/a = 0.15$) for $kb = 2.0$.

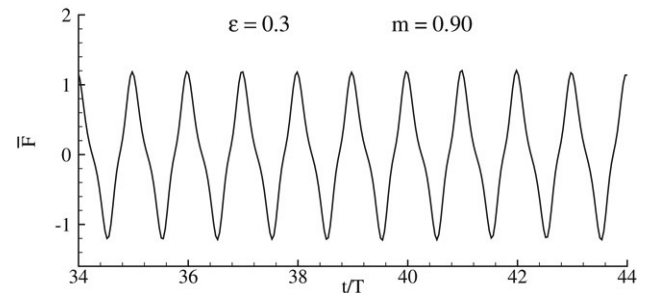


Fig. 12. Computed nondimensional cnoidal wave force on elliptical cylinder for a duration of 10 periods between $t = 34T$ and $t = 44T$ for $\epsilon = 0.3$, $m = 0.90$, and $kb = 2.0$.

computations performed in this work shows that differences in m values cause appreciable variations in force maxima. Changes in ϵ seem somewhat less effective in changing the nondimensional force maxima.

5.2. Elliptic cross-section

Cnoidal wave forces on elliptical piles are now simulated. The simulations follow the pattern established for the circular piles. Fig. 11 shows a perspective view of a cnoidal wave field with an elliptical cylinder for $kb = 2.0$ after 44 wave periods elapsed from the start. Fig. 12 depicts the nondimensional force as a function of time for $\epsilon = 0.3$ and $m = 0.90$. The thin form of the elliptical cylinder produces a wave force form which is considerably different from the form obtained in the case of circular cylinder.

In Fig. 13 computed nondimensional force values for $\epsilon = 0.1$ and for two different elliptical modulus values $m = 0.90$

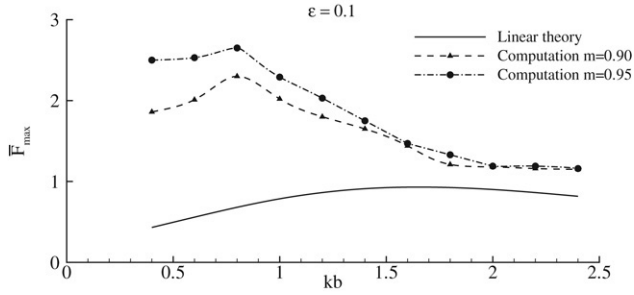


Fig. 13. Nondimensional cnoidal force maxima on elliptical cylinder for $m = 0.90$ (full triangles) and $m = 0.95$ (full circles) both for $\epsilon = 0.1$. Linear theory (solid line) is also plotted for reference.

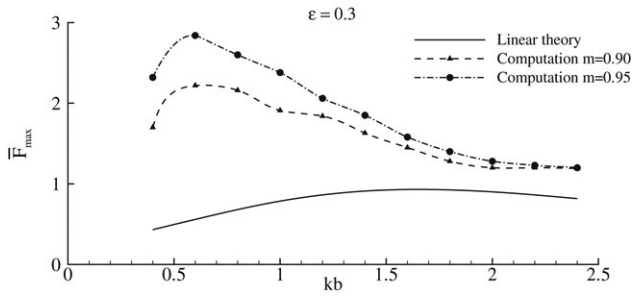


Fig. 14. Nondimensional cnoidal force maxima on elliptical cylinder for $m = 0.90$ (full triangles) and $m = 0.95$ (full circles) both for $\epsilon = 0.3$. Linear theory (solid line) is also plotted for reference.

and $m = 0.95$ are plotted along with the linear solution. The results of a corresponding simulation for $\epsilon = 0.3$ are presented in Fig. 14. Both figures show that the general conclusions drawn from Figs. 9 and 10 in Section 5.1 equally apply to the elliptical cylinders subject to nonlinear cnoidal wave loading.

6. Concluding remarks

Linear and cnoidal wave forces on vertical cylinders of circular and elliptical cross sections are numerically computed using a vertically integrated wave model in curvilinear coordinates. Computational results for linear waves compare well with the corresponding analytical values for both circular and elliptical cylinders. Simulations with cnoidal waves are performed for two different wave steepness ratios and two different elliptical modulus values to observe the effects of different nonlinearity and modulus values. While the nonlinear wave force maxima are appreciably larger than their linear counterparts in the low diffraction regime the results for the strong diffraction regime become almost identical with those of the linear theory. The change in nonlinearity does not produce dramatic differences in nondimensional force maxima while the effect of cnoidal wave form, quantified by the elliptical modulus m , is found to exert appreciable influence on the magnitude of nondimensional force. Overall the most striking feature of the simulations appear to be the strong increase in the nondimensional wave force for cnoidal waves for small kr values.

Appendix. Computing the pressure force

Details of computing the pressure force for the wave model used in this work are given below. The vertical component of the momentum equation with the use of the irrotationality condition may be written as:

$$-\frac{1}{\rho} p_z = \tilde{w}_t + \frac{1}{2}(\tilde{u}^2 + \tilde{v}^2 + \tilde{w}^2)_z + g, \quad (\text{A.1})$$

where \tilde{u} , \tilde{v} , \tilde{w} are the Cartesian velocity components in three dimensions. (A.1) may be integrated vertically in z to get

$$-\frac{1}{\rho} p = \int \tilde{w}_t dz + \frac{1}{2}(\tilde{u}^2 + \tilde{v}^2 + \tilde{w}^2) + gz. \quad (\text{A.2})$$

The wave model used in this work assumes (see Nadaoka et al. [15])

$$\begin{aligned} \tilde{u} &= \frac{\cosh k(h+z)}{\cosh kh} u, & \tilde{v} &= \frac{\cosh k(h+z)}{\cosh kh} v, \\ \tilde{w} &= -\frac{\sinh k(h+z)}{k \cosh kh} (u_x + v_y), \end{aligned} \quad (\text{A.3})$$

in which $u(x, y)$, $v(x, y)$, $w(x, y)$ are the velocity components at the still water level. Using the expressions given by (A.3) in (A.2) results in

$$\begin{aligned} -\frac{1}{\rho} p &= -\frac{\cosh k(h+z)}{k^2 \cosh kh} (u_x + v_y)_t \\ &\quad + \frac{1}{2 \cosh^2 kh} (u^2 + v^2) + gz \end{aligned} \quad (\text{A.4})$$

where use has been made of $w^2 = -\sinh^2 k(h+z)(u^2 + v^2)/\cosh^2 kh$ as obtained for periodic waves (Beji and Nadaoka, [25]). Integrating (A.4) from the bottom $z = -h$ to the surface $z = \zeta$ gives

$$\begin{aligned} \frac{1}{\rho} \int_{-h}^{\zeta} p dz &= \frac{\sinh k(h+\zeta)}{k^3 \cosh kh} (u_x + v_y)_t \\ &\quad - \frac{(h+\zeta)}{2 \cosh^2 kh} (u^2 + v^2) + \frac{1}{2} g(h^2 - \zeta^2). \end{aligned} \quad (\text{A.5})$$

The total pressure force acting on a circular cylinder in the positive x -direction is obtained by integrating around the cylinder and taking the appropriate force component:

$$\begin{aligned} \frac{F_x}{\rho} &= \frac{1}{\rho} \int_{-h}^{\zeta} \int_0^{2\pi} p r \cos \theta d\theta dz \\ &= \frac{r \sinh k(h+\zeta)}{k^3 \cosh kh} \int_0^{2\pi} (u_x + v_y)_t \cos \theta d\theta \\ &\quad - \frac{r(h+\zeta)}{2 \cosh^2 kh} \int_0^{2\pi} (u^2 + v^2) \cos \theta d\theta. \end{aligned} \quad (\text{A.6})$$

The hydrostatic pressure when integrated around the cylinder brings no contribution for being equal in all directions. The above equation may be expressed in terms of the contravariant velocities as:

$$\frac{F_x}{\rho} = \frac{r \sinh k(h + \zeta)}{k^3 \cosh kh} \int_0^{2\pi} J \left(U_{\xi}^* + V_{\eta}^* \right)_{\tau} \cos \theta d\theta - \frac{r(h + \zeta)}{2 \cosh^2 kh} \int_0^{2\pi} \left(\eta_x^2 + \eta_y^2 \right) U^{*2} \cos \theta d\theta. \quad (\text{A.7})$$

where $U^* = U/J$ and $V^* = V/J$ as indicated before. Note that the contravariant component perpendicular to the wall is zero $V = 0$. Letting $(h + \zeta) \simeq h$ and non-dimensionalizing the force gives:

$$\bar{F}_x = \frac{F_x}{\rho gh Hr (\tanh kh / kh)} = \frac{1}{gk^2 H} \int_0^{2\pi} J \left(U_{\xi}^* + V_{\eta}^* \right)_{\tau} \cos \theta d\theta - \frac{kh}{gH \sinh 2kh} \int_0^{2\pi} \left(\eta_x^2 + \eta_y^2 \right) U^{*2} \cos \theta d\theta. \quad (\text{A.8})$$

In linear computations the nonlinear second integral is neglected completely.

References

- [1] Havelock TH. The pressure of water waves upon a fixed obstacle. *Proc R Soc Lond A* 1940;963:175–90.
- [2] Omer GC, Hall HH. The scattering of a tsunami by a cylindrical island. *J Seismol Soc Amer* 1949;39(4):257–60.
- [3] MacCamy RC, Fuchs RA. Wave forces on piles: A diffraction theory. Technical memorandum no. 69. Beach Erosion Board Office of the Chief Engineers. Department of the Army; 1954. p. 1–17.
- [4] Goda Y, Yoshimura T. Wave force on a vessel tied at offshore dolphins. In: *Proc 13th coastal engng conference*. 1972. p. 1723–42 [Chapter 96].
- [5] Houston JR. Combined refraction and diffraction of short waves using the finite element method. *Appl Ocean Res* 1981;3(4):163–70.
- [6] Isaacson M, Cheung KF. Time-domain second-order wave diffraction in three dimensions. *J Waterw Port Coast Ocean Eng* 1992;118(5):496–516.
- [7] Chau FP, Eatock Taylor R. Second-order wave diffraction by a vertical cylinder. *J Fluid Mech* 1992;240:571–99.
- [8] Jiang L, Wang KH. Hydrodynamic interactions of cnoidal waves with a vertical cylinder. *Appl Ocean Res* 1996;17:277–89.
- [9] Wang KH, Ren X. Interactions of cnoidal waves with cylinder arrays. *Ocean Eng* 1999;26:1–20.
- [10] Zhu S, Moule G. An efficient numerical calculation of wave loads on an array of vertical cylinders. *Appl Math Model* 1996;20:26–33.
- [11] Stojek M, Markiewicz M, Mahrenholtz O. Diffraction loads on multiple vertical cylinders with rectangular cross section by Trefftz-type finite elements. *Comput & Structures* 2000;75:335–45.
- [12] Kyte A, Tørum A. Wave forces on vertical cylinders upon shoals. *Coast Eng* 1996;27:263–86.
- [13] Huseby M, Grue J. An experimental investigation of higher-harmonic wave forces on a vertical cylinder. *J Fluid Mech* 2000;414:75–103.
- [14] Morris-Thomas MT, Thiagarajan KP. The run-up on a cylinder in progressive surface gravity waves: Harmonic components. *Appl Ocean Res* 2004;26:98–113.
- [15] Nadaoka K, Beji S, Nakagawa Y. A fully dispersive weakly nonlinear model for water waves. *Proc R Soc Lond A* 1997;453:303–18.
- [16] Kriebel DV. Nonlinear wave interaction with a vertical circular cylinder: Wave forces. *Ocean Eng* 1998;25(7):597–605.
- [17] Boo SY. Measurements of higher harmonic wave forces on a vertical truncated circular cylinder. *Ocean Eng* 2006;33(2):219–33.
- [18] Beji S, Barlas B. Boundary-fitted non-linear dispersive wave model for regions of arbitrary geometry. *Int J Numer Methods Fluids* 2004;45: 643–57.
- [19] Korteweg DJ, de Vries G. On the change of form of long waves advancing in a rectangular canal, and on a new type of long stationary waves. *Philos Mag* 1895;39:422–43.
- [20] Mei CC. *The applied dynamics of ocean surface waves*. Singapore: World Scientific; 1989. p. 740.
- [21] Kiyokawa T, Nadaoka K, Beji S. An open boundary treatment for simulation of nonlinear wave propagation. *Proc Coast Eng JSCE* 1996; 1–5 [in Japanese].
- [22] Engquist B, Majda A. Absorbing boundary conditions for the numerical simulation of waves. *Math Comp* 1977;31:629–51.
- [23] Kantha LH, Clayson CA. *Numerical models of oceans and oceanic processes*. San Diego (CA): Academic Press; 2000. p. 940.
- [24] Abramowitz M, Stegun IA. *Handbook of mathematical functions*. New York: Dover Publications; 1972. p. 1046.
- [25] Beji S, Nadaoka K. A time-dependent nonlinear mild-slope equation for water waves. *Proc R Soc Lond A* 1997;453:319–32.